

# Natural fractures and their attributes in organic-rich shales: Insights from the Paleozoic Wufeng-Longmaxi formation, southeastern Sichuan Basin

Shijie Ma<sup>a,b</sup>, Lianbo Zeng<sup>a,b,\*</sup>, Marta Gasparrini<sup>c</sup>, Shiqiang Liu<sup>a,b</sup>, Zhikai Liang<sup>d</sup>, He Tian<sup>e</sup>, Hanyong Bao<sup>f</sup>, Wei Wu<sup>e</sup>, Liang Luo<sup>a,b</sup>

<sup>a</sup> State Key Laboratory of Petroleum Resources and Prospecting, China University of Petroleum, Beijing, 102249, China

<sup>b</sup> College of Geosciences, China University of Petroleum, Beijing, 102249, China

<sup>c</sup> University of Milan, Earth Sciences Department, via Mangiagalli 34, Milan, 20133, Italy

<sup>d</sup> Unconventional Natural Gas Institute, China University of Petroleum, Beijing, 102249, China

<sup>e</sup> Shale Gas Research Institute, PetroChina Southwest Oil and Gasfield Company, Chengdu, 610051, China

<sup>f</sup> Petroleum Exploration and Development, Jiangnan Oilfield Branch Company, SINOPEC, Wuhan, Hubei, 430223, China

## ARTICLE INFO

### Keywords:

Natural fractures

Origin

Organic-rich shale

O<sub>3</sub>W-S<sub>1</sub>l formation

Sichuan basin

## ABSTRACT

Fractures in organic-rich shale affect the evolution of permeability and control shale gas preservation. We characterize fracture attributes in the Qiyue-Huaying Fold-Thrust belt in the southeastern Sichuan Basin, revealing the distribution, origin and factors controlling fracture localization through investigation of cores, image logs, and thin section petrography. We found that the deformation intensity, organic matter content and lithology are the major factors for controlling fracture occurrence and location in the Wufeng-Longmaxi deep shale. The major fracture pattern in the Fuling Block is characterized by abundant inclined shear fractures, bed-parallel shear fractures, and bed-normal extension fractures, while bed-parallel veins prevail in the Luzhou Block. In general, fracture density and size in the Fuling Block are larger than those in the Luzhou Block. The competent layers (siliceous shale with high TOC) have the highest fracture density, and noticeably, organic matter content controls bed-parallel vein localization. Based on the distribution of fractures in two blocks, we suggest that the dominant origin of fractures in organic-rich shale gradually changes from tectonic events to fluid pressure changes due to organic maturation (organic events), from the Fuling Block to the Luzhou Block.

## 1. Introduction

An organic-rich shale usually has low host rock permeability. Consequently open fractures are, together with mineral filled fractures, important geological features that can have a dramatic impact on the mechanical strength and flow performance of hydrocarbon reservoirs in shale (Engelder et al., 2009; Cobbold et al., 2013; Gale et al., 2014; Zeng et al., 2016; Zanella et al., 2021). Additionally, pre-existing fractures can modify hydraulic fracture growth, influencing the success of engineering operations. The orientation of fractures and internal structures of mineral deposits in fractures (textures and inclusions) can reveal information about palaeo-stress fields, deformation kinematics, fracture timing, and fluid pressure (Bons et al., 2012). Therefore, characterizing the fracture attributes in deep shale is crucial to better understand brittle deformation process and permeability evolution within these potential reservoirs. On the other hand, fracture attributes can provide constraints

to calibrate numerical models for the exploration and production of unconventional resources (Romero-Sarmiento et al., 2013; Li et al., 2023). Knowledge of the attributes and origins of natural fractures is thus of practical as well as scientific interest.

Formation mechanisms and factors controlling various fracture attributes have been widely discussed. Among these concerns is the appreciation that several mechanisms may act independently or in combination to cause fractures such as diagenesis (Meng et al., 2021), hydrocarbon generation, and tectonic events (structural deformation) (Bons et al., 2012; Wilkins et al., 2014; Zanella et al., 2015; Zeng et al., 2016; Caswell and Milliken, 2017; English and Laubach, 2017).

Previous studies have reported that in shale the dominant location of fractures mainly depends on the Young's modulus and Poisson's ratio or brittleness (e.g. lithology), as well as the stratigraphic contrast between beds (Engelder and Peacock, 2001; Peacock and Mann, 2005; Zeng et al., 2013; Ilgen et al., 2017; Peng et al., 2020).

\* Corresponding author. State Key Laboratory of Petroleum Resources and Prospecting, China University of Petroleum, Beijing, 102249, China.

E-mail address: [lbzeng@sina.com](mailto:lbzeng@sina.com) (L. Zeng).

<https://doi.org/10.1016/j.jsg.2024.105197>

Received 31 August 2023; Received in revised form 17 June 2024; Accepted 25 June 2024

Available online 27 June 2024

0191-8141/© 2024 Elsevier Ltd. All rights reserved, including those for text and data mining, AI training, and similar technologies.

For organic-rich shale, fluid overpressure has been regarded as a major opening force for extensive fracturing and an effective driving force for oil and gas migration (Hunt, 1990; Hantschel and Kauerauf, 2009; Fall et al., 2012). Previous studies have reported a correlation between the formation of bed-parallel veins and overpressure during hydrocarbon generation (Cobbold et al., 2013). Therefore, many datasets document a positive correlation between TOC and BPV localizations (Larmier et al., 2021). However, this correlation is not always universal, such as TOC seem have a low correlation between BPV locations (Weger et al., 2019). This is interpreted that weak interfaces provided by abrupt lithology changes can control the BPV location (Larmier et al., 2021).

These considerations show that to understand the distribution of fractures, the effects of structural position and rock type need to be accounted for. Moreover, since uplift history may also play a role in fracture development (English and Laubach, 2017) studies that focus on fractures at depth have the advantage of minimizing the effect of this variable. Here, we use core to investigate fractures in an organic shale that is found in different structural blocks in an active tectonic setting.

The Sichuan Basin is a major shale gas production area in China (Ma and Xie, 2018; Ma et al., 2020). Fractures have garnered considerable attention for their effects on the storage and migration of natural gas in the Upper Ordovician Wufeng Formation-Lower Silurian Longmaxi Formation (439–444 Ma) (Zeng et al., 2013, 2021; Xu et al., 2021; Tian et al., 2022; Ma et al., 2023). The current exploration in the southeastern Sichuan Basin shows that with a similar hydrocarbon generation potential and burial history, there is significant heterogeneity in gas reserves and production (Zou et al., 2015; Ma et al., 2020). Previous studies have shown that the fold/fracture deformation process related to uplift since Yanshanian has affected the leakage of shale gas (Liu et al., 2021; Ma et al., 2021; Feng et al., 2022). Physical simulations combined with apatite fission track show that deformation intensity decreases from the basin margin to the interior in southeastern Sichuan Basin (Li et al., 2020; Feng et al., 2022). This implies that regional variation in deformation intensity and associated fluid pressure may lead to different fracture attributes in different blocks.

Because it is impossible to detect or adequately characterize fractures using geophysical data, fracture characterization of deep (2000 m–5000 m) core is important to better understand the brittle structure in shale (Table 1). However, few published studies exist on natural fracture attributes in the Wufeng-Longmaxi Shale (Xu et al., 2020; Li et al., 2024), although fractures are common.

In this study, we investigate the attributes and distribution of fractures in organic-rich shale in the southeastern Sichuan Basin (Fig. 1). The main purposes of this survey were: 1) to constrain the factors controlling fracture occurrence in organic-rich shale, 2) to define the fracture attributes in deep shale, in order to determine the heterogeneous distribution of fractures in different structural blocks and to assess the

causes of this variability. For this organic-rich shale, we show that the cause of fractures shifts spatially across structural blocks from tectonic events to fluid pressure changes due to organic maturation (organic events).

2. Geological setting

The Sichuan Basin is a large petroliferous basin in the South China block (Fig. 1a) containing abundant shale gas resources in the Wufeng-Longmaxi formation (Zou et al., 2021), which has undergone multi-stage subsidence, uplift, and exhumation since the Proterozoic. The Sichuan basin is dominated by three stages of basin evolution: (a) a marine carbonate platform from the Ediacaran to Middle Triassic, (b) a foreland basin with fold deformation from the Late Triassic to Late Cretaceous, and (c) subsequent exhumation uplift and structural adjustment from the late Cretaceous to the Quaternary (Deng et al., 2016; Liu et al., 2021).

Our focus is the southeast of the Sichuan Basin, and the deformation that propagated from the Yangtze block into the southeast Sichuan Basin through a flat-ramp-flat structure (He et al., 2018; Gu et al., 2021), with a boundary at the Qiyue thrust (Fig. 1a and b). A remarkable structural feature is the multiple reverse fault groups with different trends. The strike of the major fault rotated from northeast to north-south and formed a large, broom-like thrust belt (Fig. 1b). Since the Paleozoic, the southeast Sichuan Basin has undergone several tectonic events during Yanshanian to Himalayan Orogeny (Liu et al., 2021), expressed by at least two phases of deformation from Late Cretaceous to Oligocene. The first one is characterized by the NE-striking reverse faults formed during the Yanshanian Orogeny (Fig. 1c). A second nearly E-W compressional stage is visible with nearly SN-striking reverse faults formed during the Himalayan Orogeny (Fig. 1d) (Cao et al., 2023).

The shales studied belong to Upper Ordovician Wufeng (O<sub>3w</sub>) and the First Member of the Longmaxi (S<sub>1l</sub>) Formations (439–444 Ma) (Fig. 2a). During the deposition of the O<sub>3w</sub>-S<sub>1l</sub> Formation, the study area was in a large bay environment with low energy and hypoxia. (Huang et al., 2018; Zhang et al., 2018), and the total thickness of the targeted layers is from 80 to 150 m. A previous study reported that four geological events control the deposit of the O<sub>3w</sub>-S<sub>1l</sub> Formation, including glaciation, volcanic eruptions, the Kwangsi Orogeny, and turbidity currents (Huang et al., 2023) (Fig. 2b), which results in the obvious three-part subdivision of the target layer (Fig. 2b). The bottom interval of O<sub>3w</sub>-S<sub>1l</sub> Formation is mainly black carbonaceous and siliceous shale, containing massive siliceous biological fossils like radiolarians and siliceous sponges. The middle interval is mainly gray-black and black silty shale. The siliceous components here are mainly terrestrial silts with rare biological fossils. The top interval is mainly gray and dark gray clay shale, while siliceous content is low (<50%) (Guo, 2019).

Table 1  
Summary of information about survey wells in the study area.

Location	Well	Samples	Core length [m]	Depth range [m]	Ro [%]		TOC [%]	Pore fluid factor (λ)
Luzhou	L1	106	121	3921.4–4042.4	2.8	Min-Max	0.18–4.97	0.90
						Avg-	1.61	
	L2	118	103.3	3950.7–4054	2.8	Min-Max	0.14–5.04	0.84
						Avg-	1.88	
	L3	163	169.7	3296.2–3465.9	2.8	Min-Max	0.11–6.62	0.81
						Avg-	1.56	
Fuling	F1	84	99	4562–4661	2.8	Min-Max	0.24–5.55	0.52
						Avg-	2.33	
	F2	129	121	3486.3–3607.3	2.8	Min-Max	0.11–7.42	0.48
						Avg-	2.05	
	F3	107	115.3	3395.5–3510.8	2.8	Min-Max	0.19–4.69	0.41
						Avg-	2.01	
	F4	101	142.3	2134–2276.3	2.8	Min-Max	0.31–6.81	0.50
						Avg-	2.45	
	F5	32	94.6	2804–2898.6	2.8	Min-Max	0.33–4.81	0.41
						Avg-	2.38	

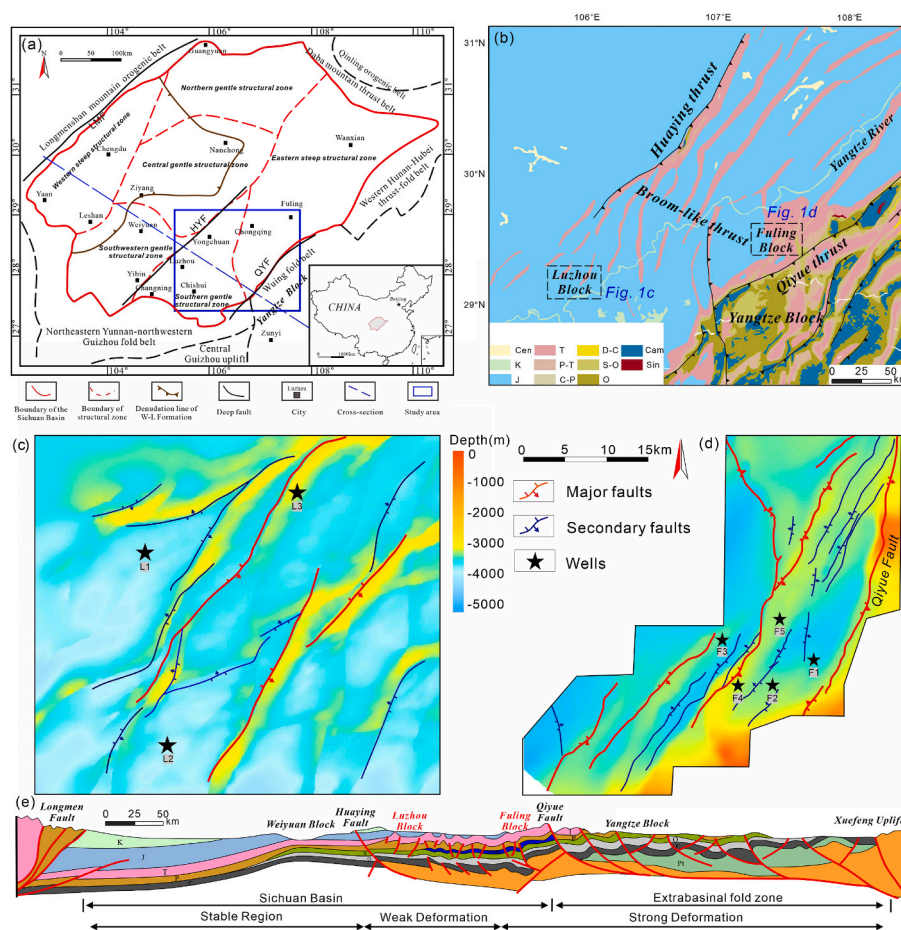


**Fig. 1.** Geology of the Qiyue-Huaying Fault-Thrust belt. (a) Location of the study area (the blue rectangle) and tectonic units of the Sichuan Basin modified from (Dai et al., 2014). HYF-Huaying fault, QYF-Qiyue fault. (b) Geological map of the Sichuan Basin with the Upper Ordovician Wufeng Formation-Lower Silurian Longmaxi Formation ( $O_3w-S_1l$ ) outcrops along the Qiyue-Huaying Fold-Thrust belt. Only major thrust fault distributions are shown. (c) Location of wells in Luzhou Block. (d) Location of wells in Fuling Block. (e) Simplified cross section across the Sichuan Basin from NW to SE, including the Longmen orogenic belt in the NW, Xufeng uplift domain in the SE, the western and central Sichuan Basin, and the southeastern Sichuan Basin which is bounded by the Huaying fault and Qiyue fault. (For interpretation of the references to color in this figure legend, the reader is referred to the Web version of this article.)

From the bottom to the top, the targeted layers generally transit from deep-water shelf facies to shallow water shelf facies, displaying lighter color, decreasing TOC, fewer siliceous minerals, and increasing clay content (Tuo et al., 2016; Hao et al., 2021).

In general, the burial history of the target layer is characterized by early subsidence and late uplift. According to basin modeling (Gao et al., 2019), rapid subsidence during the Triassic and Jurassic with a maximum burial (about 7000 m) during the Cretaceous was followed by significant uplift, erosion, and deformation during the Yanshanian-Himalayan orogeny (after Late Cretaceous) (Ge et al., 2016; Li et al., 2020). The main phase of oil generation began in the Triassic, before maximum burial in the Late Cretaceous, and peaked during the Early Cretaceous (Shangbin et al., 2017). During the Late Cretaceous, the depth to the bottom of the  $O_3w-S_1l$  Formation was nearly 7000 m, which led to black shale becoming overmature ( $R_o > 2.5\%$ ) (Liu et al., 2016). The study area experienced continuous uplift from the Later Yanshanian to Himalayan. At present, the burial depths of the  $O_3w-S_1l$  Formation mainly range from 2500 m to 4500 m, with more shallowly buried rocks near the basin margin. All rocks are in the late stage of oil cracking.

### 3. Methodology and data

#### 3.1. Mineralogy and organic matter measurements

Our study is based on cores from eight vertical wells located in the Qiyue-Huaying Fold-Thrust belt in the southeastern Sichuan Basin. Core lengths range from 94.6 to 169.7 m and total length of 966.2 m (Table 1). Five wells are in the strong deformation area near the edge of the basin (Fuling Block), and three wells are in the weak deformation area near the basin interior (Luzhou Block) (Fig. 1b). To find potential links between the fractures and host-rock petrophysical properties, for eight cores, Rock-Eval analysis and X-ray diffraction (1-m spacing) were used to measure TOC (TOC<sub>lab</sub>) and quantitative mineralogy (Weger et al., 2019; Ravier et al., 2020; Larmier et al., 2021). Results are expressed as a discrete dataset related to depth (Fig. 3, Fig. 4). A total of 840 XRD measurements and Rock-Eval analyses were made in this study (Table 1). Furthermore, to constrain the relationship between fracture locations and TOC value, continuous TOC values (TOC<sub>log</sub>) quantified by resistivity and porosity logs are compared with fracture locations.

#### 3.2. Drill observations and fracture measurement

Structures of interest in the cores are fractures (opening-mode fractures that are open or mineral filled, in other words, joints and veins) that are visible to the eye, rather than micro-fractures and faults. The

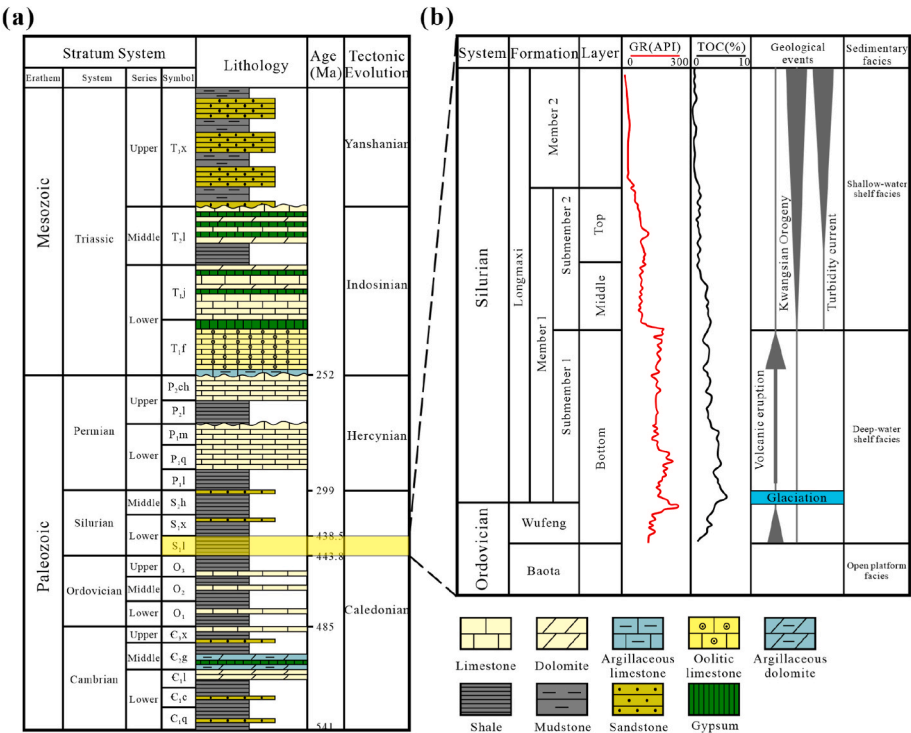


Fig. 2. Simplified stratigraphic column for the southeastern Sichuan Basin (a) and the sequence of geological events (b) in the Wufeng-Longmaxi Formation, modified from (Huang et al., 2023).

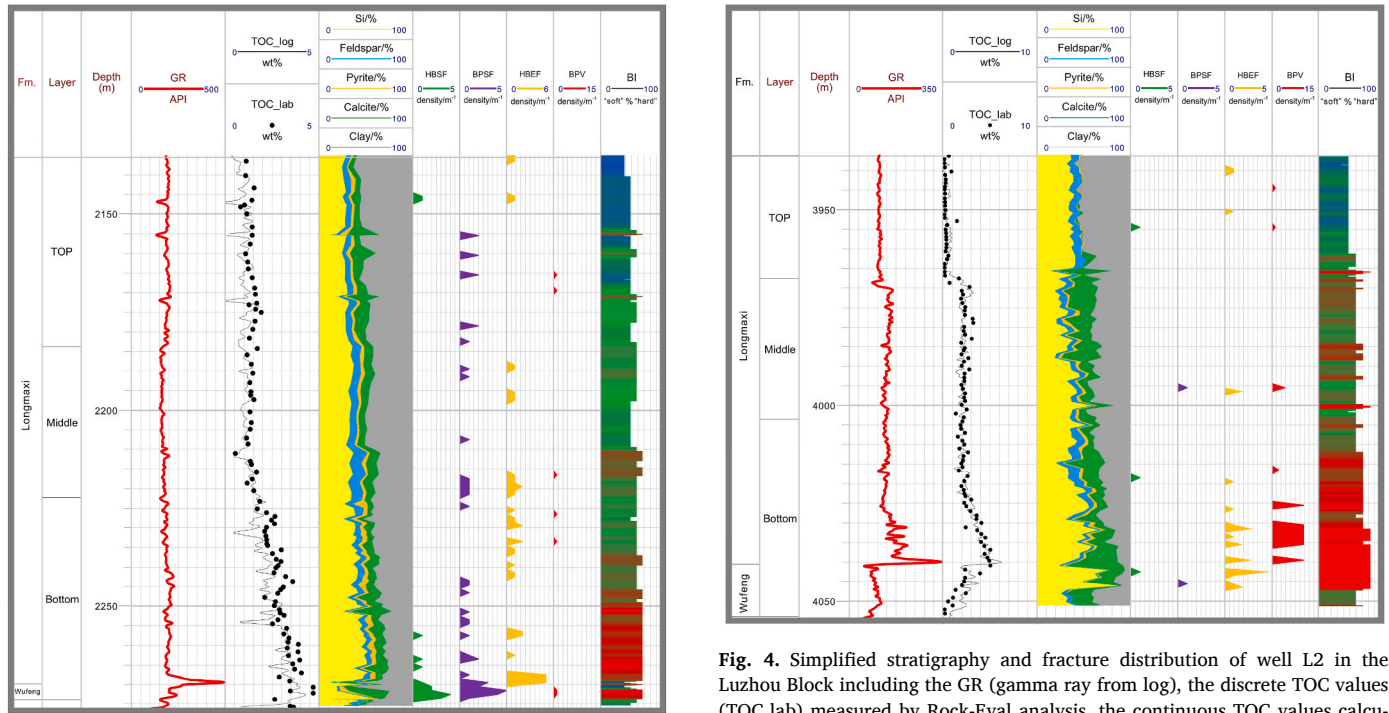


Fig. 3. Simplified stratigraphy and fracture distribution of well F4 in the Fuling Block including the GR (gamma ray from log), the discrete TOC values (TOC\_lab) measured by Rock-Eval analysis, the continuous TOC values calculated by log curve, calculated by XRD data, the density ( $m^{-1}$ ) of four types of fractures, and brittleness. BI-brittleness index. High values of brittleness are in red, low values in blue, intermediate values are in green. (For interpretation of the references to color in this figure legend, the reader is referred to the Web version of this article.)

Fig. 4. Simplified stratigraphy and fracture distribution of well L2 in the Luzhou Block including the GR (gamma ray from log), the discrete TOC values (TOC\_lab) measured by Rock-Eval analysis, the continuous TOC values calculated by log curve, calculated by XRD data, the density ( $m^{-1}$ ) of four types of fractures, and brittleness. BI-brittleness index. High values of brittleness are in red, low values in blue, intermediate values are in green. (For interpretation of the references to color in this figure legend, the reader is referred to the Web version of this article.)

observations were limited to small-scale structures by full core size of 100cm/10cm/10 cm archived in boxes. Attributes measured on image logs, cores, and thin sections include the following: (1) fracture type,



orientation, and depth on cores; (2) fracture strike measured by image log; (3) heights of inclined shear fractures and bed-normal extension fractures in cores. Most of the truncated fractures are inclined shear fractures in cores. Note that even though truncated, minimum heights can be measured. Also documented are (4) cement texture; (5) the fracture density ( $\text{m}^{-1}$ ).

## 4. Results

### 4.1. TOC and mineralogy

The O<sub>3</sub>w-S<sub>1</sub>l Formation is dominated by type I kerogen and represents a narrow range from 2.8% to 3.0 % Ro in study area (Dai et al., 2014). The TOC of the Luzhou Block ranges from 0.14% to 5.04 %, with an average of 1.88% (Fig. 5a). The TOC of the Fuling Block ranges from 0.31% to 6.81 %, with an average of 2.45 %. Generally, the TOC content shows wide variations between these three intervals, with a general order of Top < Middle < Bottom (Fig. 5b). The TOC at the bottom interval is almost more than 3 %, and the TOC shows a decreasing trend in the vertical direction and is the lowest at the top interval (Figs. 3 and 4).

The main components of shale are quartz and clay minerals, accounting for about 80% (Fig. 6a), followed by carbonate minerals (such as calcite and dolomite) and feldspar, while pyrite is only present in small quantities. A ternary diagram of mineralogy (Lazar et al., 2015) shows that most of the shale samples can be classified into three main groups, namely siliceous lithofacies (si), argillaceous-siliceous mixed lithofacies (ar-si and si-ar) and argillaceous lithofacies (ar) (Fig. 7a). The top interval of the Wufeng-Longmaxi Formation is mainly composed of argillaceous shale, while the middle and bottom interval are dominated by argillaceous-siliceous mixed shale (ar-si and si-ar) and siliceous shale, respectively (Fig. 7b). Overall, the quartz content increases with increasing depth, while the clay content decreases (Figs. 3 and 4). Thus, these three intervals were further divided into organic-poor argillaceous lithofacies, organic-containing argillaceous-siliceous mixed lithofacies, and organic-rich siliceous lithofacies, based on the mineral composition and TOC content.

Rock brittleness is the tendency of rock brittly failing when it is subjected to stress. Brittleness has a strong effect on the occurrence of fractures. In our study, the content of brittle minerals (quartz, feldspar, pyrite, and carbonate minerals) is used to calculate a brittleness index (BI) (Pei et al., 2016).

The brittleness index of the Luzhou Block ranges from 41 % to 87 %, 63 % on average; The brittleness index of the Fuling Block ranges from 33 % to 78 %, 58 % on average. Overall, the brittleness index in the Luzhou Block is slightly higher than that in the Fuling Block. Note that the brittleness index gradually decreases from the bottom interval to the top interval (Figs. 3, 4 and 6b) and the content of quartz at the bottom

interval can exceed 75 %, which is related to extensive siliceous fossils. This variation can be interpreted as the biological quartz gradually becoming sparse upward, where terrigenous inflow deposits tend to be dominant (Huang et al., 2023). In the bottom interval, volcanic and glacial events contributed to high productivity and anoxic water, resulting in organic-rich shale with abundant k-bentonite and pyrite layers (Huang et al., 2023).

Generally, the frequent volcanic events and deep-water shelf with low terrigenous supplied organic matter and siliceous skeletons to the bottom interval of the O<sub>3</sub>w-S<sub>1</sub>l Formation sediments (Huang et al., 2023). However, subsequent sediments (middle and top interval) with low organic matter are the result of the rapid sedimentary rate and elevated terrigenous materials (detrital quartz and clay minerals) related to Kwangshian Orogeny.

### 4.2. Fracture characterization

#### 4.2.1. Fracture types and vein petrography

Based on the investigation of the core and thin sections, combined with fractography, four main types of fractures are identified, including the following:

- (1) Inclined shear fractures (ISFs) are commonly non-strata-bounded and always steeply dipping fractures (dip angle >70°) (Fig. 8a–c). The fracture surfaces are decorated with glassy or striated calcite created by significant shear offset (Fig. 8a and b), indicating its shear slip mechanism. These fractures are commonly sealed with stretching calcite crystal and pyrite (Fig. 9a and b), indicating mixed failure mode. Due to the limitation of core diameter (100cm/10cm/10 cm), high angle to bedding shear fracture lengths are censored. The height in core ranges from decimeters to meters.
- (2) Bed-parallel shear fractures (BPSFs) are parallel or sub-parallel to bedding planes. On the fracture surfaces there are slickensides decorated with scratches and steps (Fig. 8d), indicating the mixed failure mode. Such fractures are frequently sealed with fibrous calcite formed by crack-seal events (Figs. 8e and 9c). These structures have inclusion bands of wall-rock fragments (Fig. 9c). Such textures in mineral-filled fractures typically record evidence of many repeated cycles of shear fracturing and cement precipitation (Ramsay, 1980; Laubach et al., 2004; Holland and Urai, 2010).
- (3) Bed-normal extension fractures (BNEFs) are generally strata-bounded (Hooker et al., 2013), and the fracture height is controlled by mechanical layering (Fig. 8f), fracture terminations commonly occur at lithologic interfaces (Fig. 8f), suggesting a difference in the strain response of lithologies or interfaces.

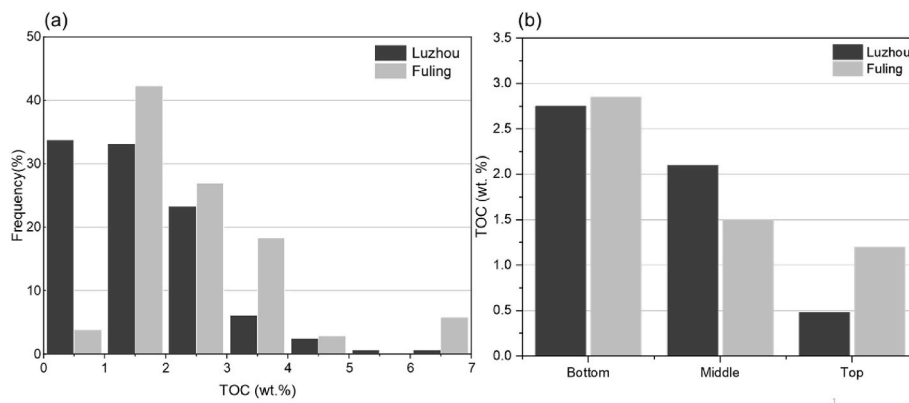


Fig. 5. Comparison of the total organic carbon between two blocks. (a) The distribution frequency of TOC. (b) The average TOC of three intervals of the O<sub>3</sub>w-S<sub>1</sub>l Formation.

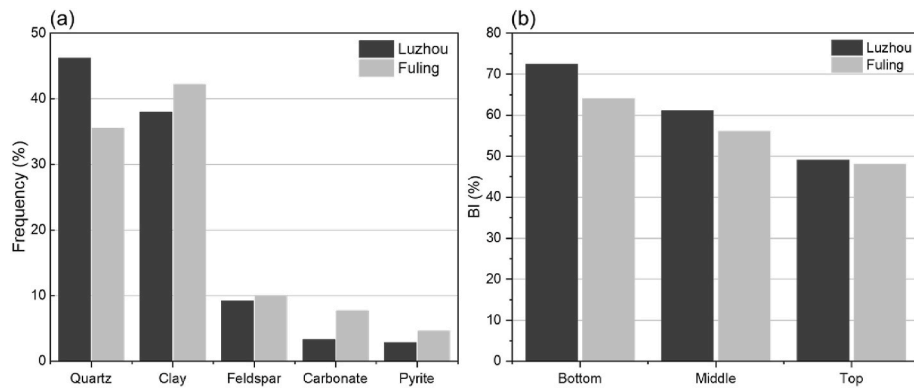


Fig. 6. Comparison of mineralogy between the two blocks. (a) The proportion of different types of minerals. (b) The brittleness index of three intervals of the O<sub>3</sub>W-S<sub>1</sub>l Formation.

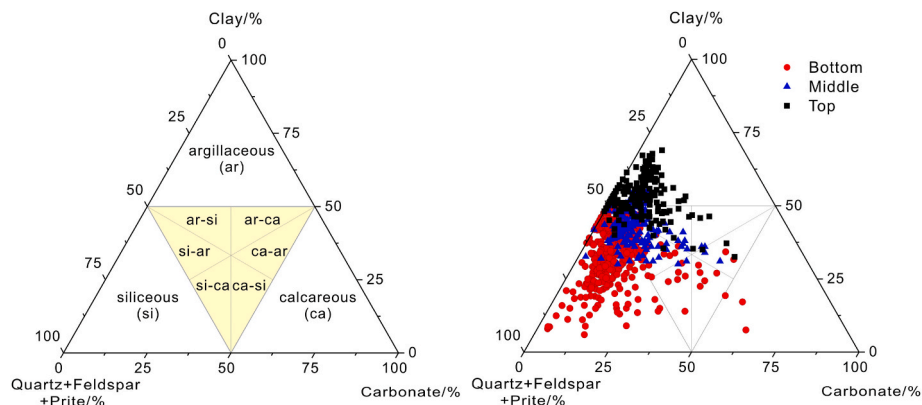


Fig. 7. (a) Classification of shale lithofacies adapted from (Lazar et al., 2015); (b) Ternary plots of the mineralogy of the shale in the Wufeng-Longmaxi Formation based on X-Ray Diffraction analysis; si– siliceous; ca–calcareous; ar–argillaceous.

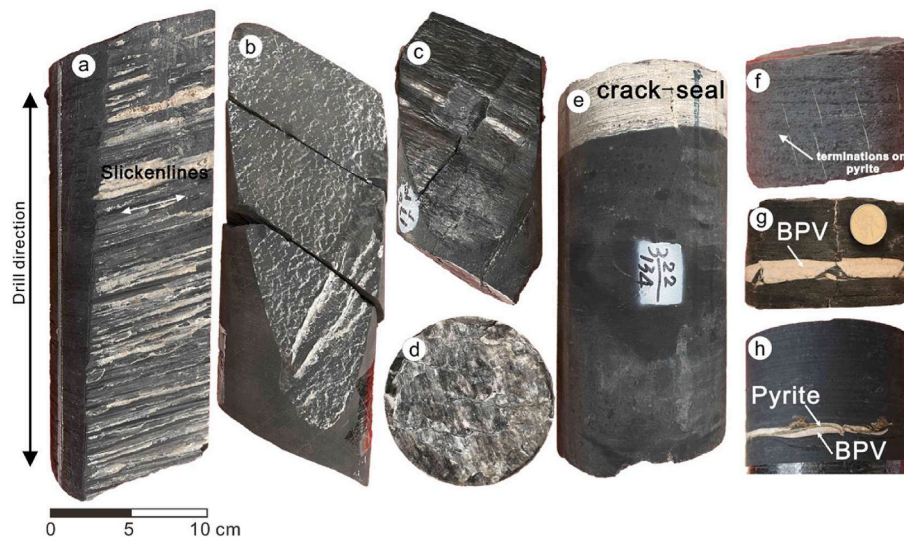
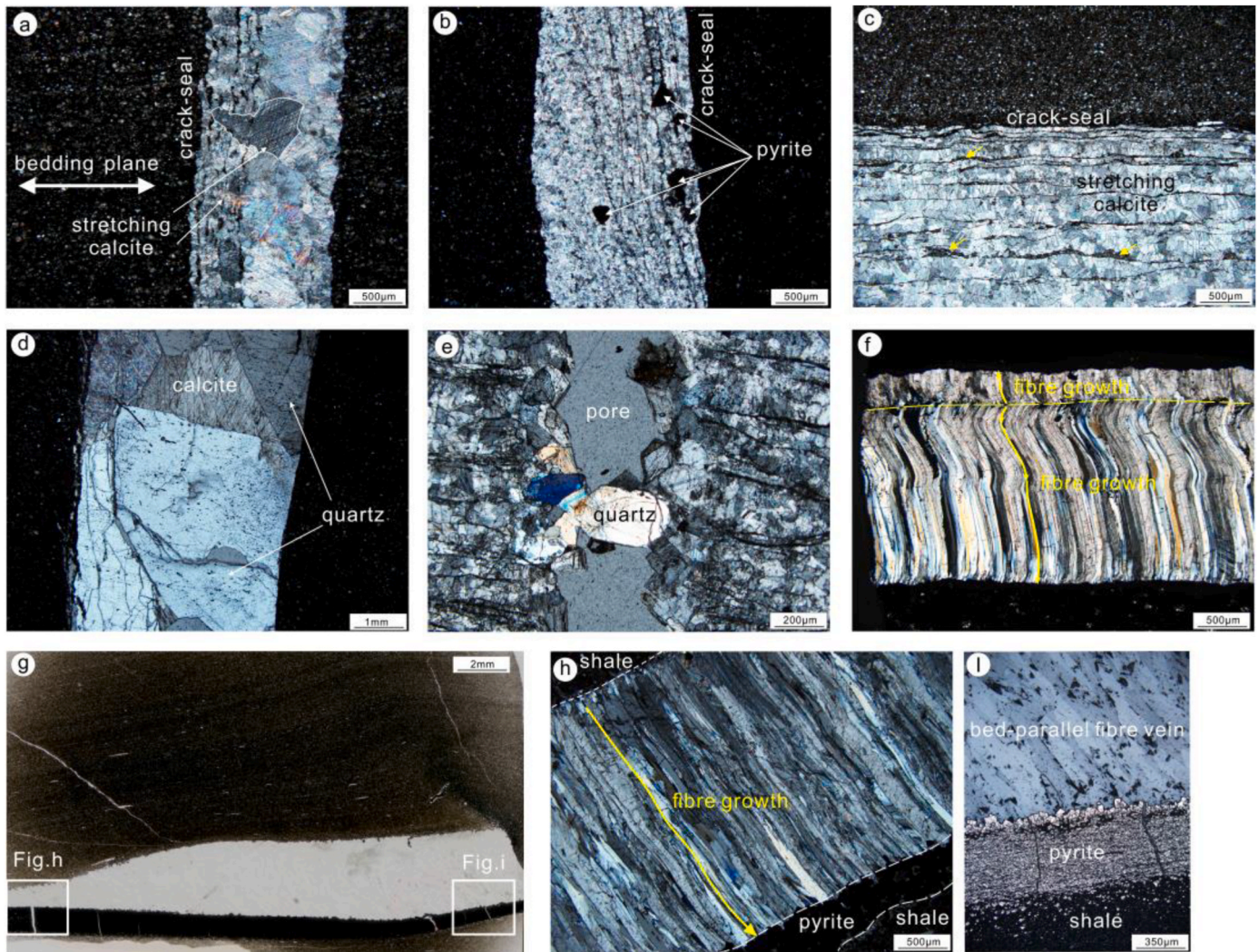


Fig. 8. Photography of the fractures in cores. (a–b) Inclined shear fracture (dip angle > 70°), the stepped calcite crystal slickensides along steep shear fractures face, representing mixed mode failure. (c) Inclined shear fracture, glossy slickensides along steep shear fractures face, may represent mode II failure. (d) Top projection of the sample-E. Bed-parallel shear fracture, stepped crystal-fiber slickensides along bedding plane, representing mixed mode failure. (e) Mineralized bed-parallel shear fracture exceeding 5 cm recorded multiple crack-seal events and represent mixed mode failure. Note that bed-normal extension fracture cuts through bed-parallel fibrous veins, representing mode I failure and vertical opening. Fractures terminate in thin pyrite layers. (g–h) Bed-parallel fibrous veins, representing mode I failure and vertical opening.





**Fig. 9.** Petrography of fractures. (a–b) Calcite with evidence of minor stretching episodes marked by fracture-wall-parallel inclusion bands as well as blocky minerals with jagged edges. Dispersed pyrite microcrystals occur locally in the veins. (c) Calcite with parallel inclusion bands, indicating vertical opening and about one dozen crack-seal events. The inclusion bands are fragments from wall-rock (yellow arrows) (d) Opening sealed with blocky calcite and quartz crystal. (e) Partly mineralized bed-normal tensile fractures cross pre-existing bed-parallel shear fracture. (f) Minor coarsening of the smooth fibres indicate the growth direction and can record the opening trajectory. (g–h) Fibrous vein where the fibres are seeded on a layer of pyrite, but not on a median zone. (i) The transmitted light photo of a fibrous vein seeded on a layer of pyrite. (For interpretation of the references to color in this figure legend, the reader is referred to the Web version of this article.)

Fracture terminations at boundaries may be abrupt or tapering. The bed-normal extensional fractures are sealed with blocky or elongated blocky calcite and quartz crystals (Fig. 9d), while some fractures are partly mineralized by quartz crystals (Fig. 9e). Our observations suggest that the bed-normal fractures opened in mode I in most cases.

- (4) Bed-parallel mineral filled fractures are generally mineralized by fibrous calcite (calcite beef) in our study area (Fig. 8g and h), which is common for fractures in organic-rich shale of marine-carbonate origin (Cobbald et al., 2013; Gale et al., 2014). These fractures are widely referred to as bed-parallel veins (BPVs), and we adopt this terminology. Some BPVs show fibers perpendicular to the edges of the host rock, indicating that they are formed by a pure extensional opening. Some others show sigmoidal fibers (Fig. 9f) that record structural shortening during their growth (Rodrigues et al., 2009; Ukar et al., 2017). Not all bed-parallel veins crosscut the whole core, some of them are the same length as bed-parallel pyrite strips (Fig. 8h), in which fibers seem to have grown from one edge to another without a median zone (Fig. 9g–i).

#### 4.2.2. Characterization of fracture attributes

The datasets (Fig. 10) show that the density of inclined shear fractures in the weak deformation area (Luzhou block near the basin interior) are relatively low, ranging from  $0.02 \text{ m}^{-1}$  to  $0.09 \text{ m}^{-1}$ , with an average of  $0.05 \text{ m}^{-1}$ . The bed-parallel veins have the highest abundance, ranging from  $0.09 \text{ m}^{-1}$  to  $0.60 \text{ m}^{-1}$ , with an average of  $0.40 \text{ m}^{-1}$ . The bed-normal extension fractures range from  $0.16 \text{ m}^{-1}$  to  $0.20 \text{ m}^{-1}$ , with an average of  $0.18 \text{ m}^{-1}$ . The bed-parallel shear fractures range from  $0.13 \text{ m}^{-1}$  to  $0.20 \text{ m}^{-1}$ , with an average of  $0.17 \text{ m}^{-1}$ .

Contrarily, the density of inclined shear fractures in strong deformation area (Fuling block near basin margin) are abundant, ranging from  $0.02 \text{ m}^{-1}$  to  $0.16 \text{ m}^{-1}$ , with an average of  $0.09 \text{ m}^{-1}$ ; The bed-parallel veins range from  $0.05 \text{ m}^{-1}$  to  $0.20 \text{ m}^{-1}$ , with an average of  $0.09 \text{ m}^{-1}$ ; The bed-normal extension fractures range from  $0.18 \text{ m}^{-1}$  to  $0.36 \text{ m}^{-1}$ , with an average of  $0.25 \text{ m}^{-1}$ ; The bed-parallel shear fractures range from  $0.28$  to  $0.38$ , with an average of  $0.34 \text{ m}^{-1}$ .

In general, bed-parallel veins are abundant in the Luzhou block, while three other types of fractures are more developed in the Fuling block. Additionally, we notice that the fractures at the bottom interval of the  $\text{O}_3\text{w-S}_1\text{l}$  Formation have distinctly increased compared with the

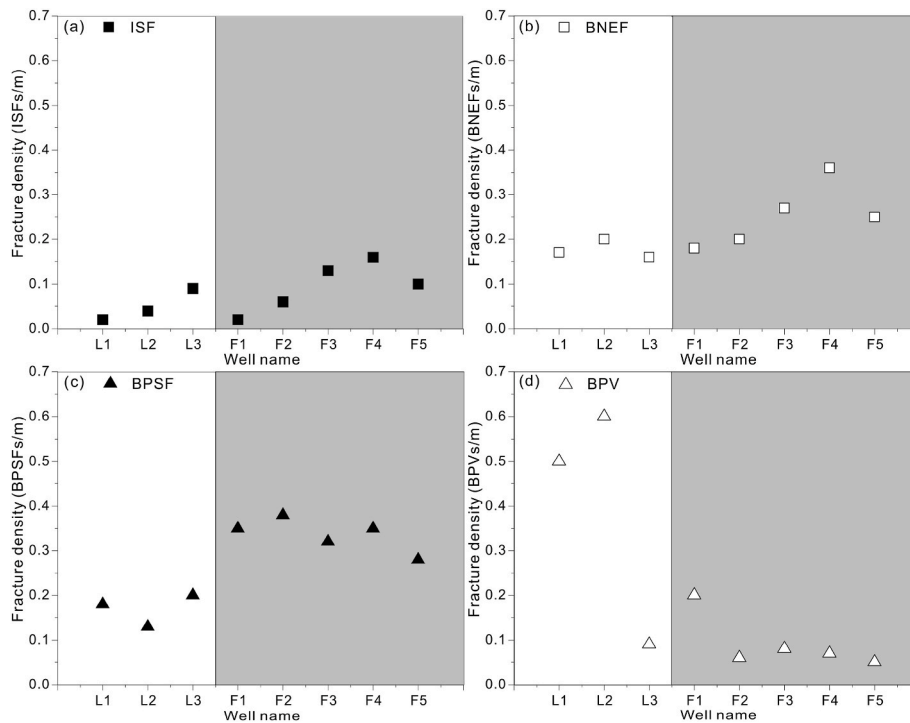


**Fig. 10.** Comparison of fracture density in eight cored deep wells. (a) The density of inclined shear fractures per well. (b) The density of bed-normal extension fractures per well. (c) The density of bed-parallel shear fractures per well. (d) The density of bed-parallel veins per well.

middle and top interval (Figs. 3 and 4). This shows that the localization of fractures may be controlled by lithology. Fractures are more abundant in siliceous shale with high TOC in the Wufeng-Longmaxi Formation.

The data (Fig. 11, Fig. 12) suggest that the height and orientation of BNEFs and ISFs differ between the two blocks. For such fractures, the measured fracture heights of the Fuling Block are larger than that of the Luzhou Block (Fig. 11). The fracture pattern is characterized by large-scale and steeply dipping shear fractures in the Fuling Block (Fig. 11a

and b), contrarily, small-scale fractures and abundant BPVs in the Luzhou Block (Figs. 10 and 11c and d). Bed-normal extension fractures strike NWW, with subsidiary NNE-striking counterparts, trending perpendicular or parallel to the fold axis direction (Fig. 12a). Note that large-scale BNEFs are dominantly EW-striking and occur in the Fuling Block (Fig. 12b). For inclined shear fractures, they are dominantly NNW-striking in the Luzhou Block (Fig. 12c), however, additional NNW-striking and NEE-striking in the Fuling Block (Fig. 12d).

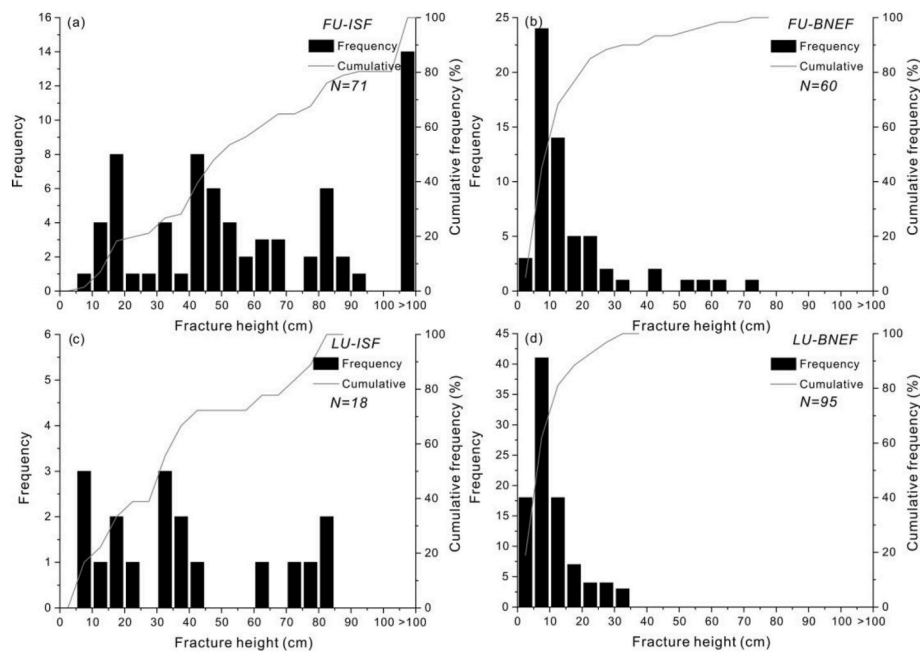


**Fig. 11.** Distribution of the number of fracture heights. (a–b) The number distribution of ISF (a) and BNEF (b) heights in the Fuling Block. Note that ISFs are commonly truncated on the core, and the fracture heights indicate the minimum heights, while the BNEF heights are the real heights. (c–d) The number distribution of ISF (c) and BNEF (d) heights in the Luzhou Block.



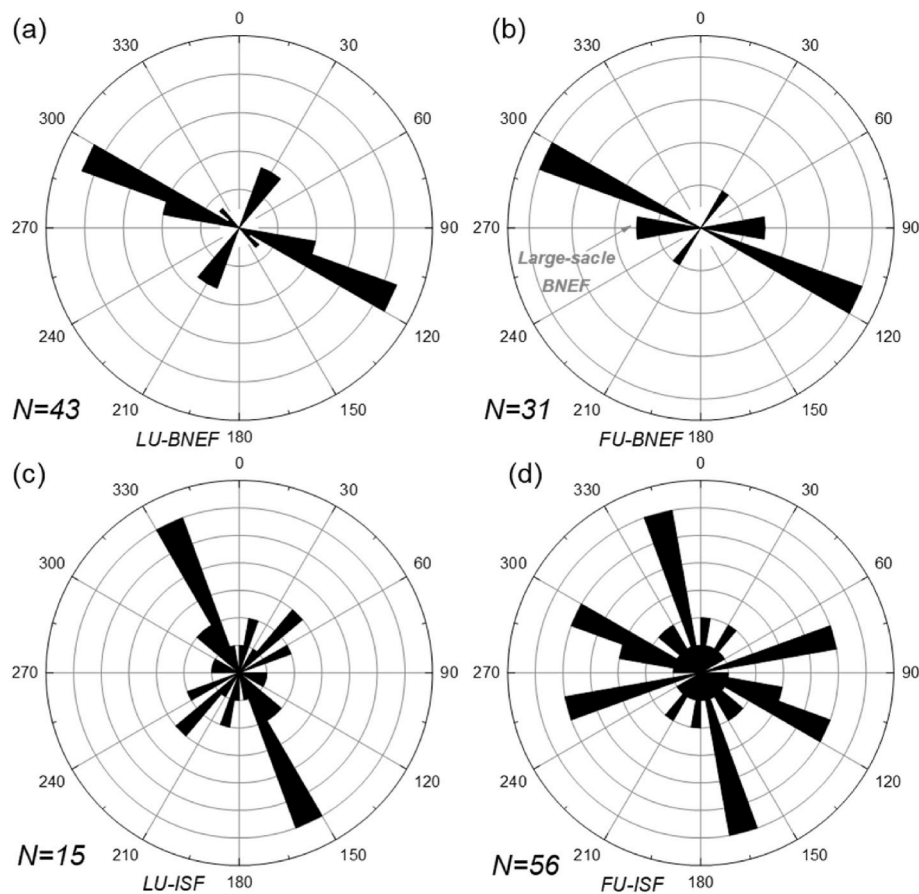


**Fig. 12.** Rose diagrams showing fracture strikes in the core. (a–b) The bed-normal extension fracture orientation. Note that EW-striking BNEFs in the Fuling Block are mainly large-scale fractures. (c–d) The inclined shear fracture orientation.

## 5. Discussion

### 5.1. Host-rock control on fracture localization

The influence of TOC and rock brittleness on the fracture density of shale is debated. In the Longmaxi and Nunitang Shale the TOC and rock brittleness show a positive correlation with the fracture abundance (Zeng et al., 2013; Xu et al., 2021; Zhang et al., 2023). Conversely, host-rock TOC seems not to be correlated with the fracture density (Gasparrini et al., 2021). This is interpreted to be related to vertical facies heterogeneity and locally specific carbonate diagenetic phases. The localization of fractures in organic-rich shale may be controlled by factors governing the mechanical stratigraphy (Laubach et al., 2009). Factors include the composition of shale (e.g. mineralogy, organic carbon content), and their sedimentary features (e.g. bedding thickness, interface frequency, and mechanical contrast) (Hooker et al., 2013; Zeng et al., 2016; Meng et al., 2018; Xu et al., 2021), which determine the mechanical properties.

Rock brittleness is the key criterion for determining the most suitable intervals for fracture advantage localization. The brittleness can be evaluated based on lithology (Pei et al., 2016). The shale lithology exerts a first-order control on brittleness, and therefore on shale fracturing. The content of hard minerals (such as quartz, feldspar, carbonate, and pyrite) which have high the Young's modulus has been found to be positively correlated with brittleness and fracture density of shale (Labani and Rezaee, 2015; Wang et al., 2017). Conversely, high clay content makes shale more ductile. Therefore, the brittleness of shale can be predicted based on the volume percentage of quartz, feldspar, carbonate content, and pyrite, by calculating its brittleness index based on mixture rules (Pei et al., 2016).

The fracture densities of the three intervals were compared (Fig. 13). Due to the potential relationship between organic matter content and BPV. Such fracture densities incorporate only inclined shear fractures, bed-parallel shear fractures, and bed-normal extension fractures combined together. The bottom interval has the highest fracture abundance, ranging from 0.76 m<sup>-1</sup> to 1.56 m<sup>-1</sup>, with an average of 1.07 m<sup>-1</sup>, while the middle and top intervals are relatively barren in the same wells (Figs. 3,

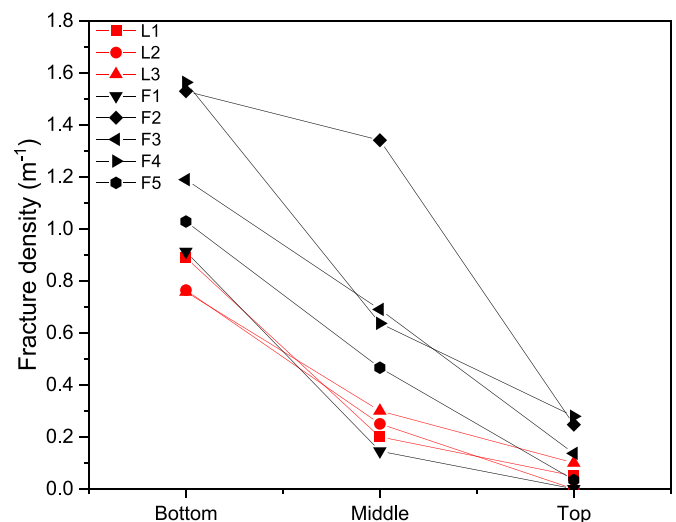


**Fig. 13.** Shows the average fracture density of three intervals in the O<sub>3</sub>w-S<sub>1</sub>l Formation. The fracture density includes inclined shear fractures, bed-parallel shear fractures, and bed-normal extension fractures combined together.

Fig. 4, Fig. 13).

Siliceous shales that have high brittleness and preferentially fracture under the stresses that may not deform other shales. Such layers may be considered competent since adjacent layers may remain undeformed or deform dustily (flow). The content of hard minerals determines the mechanical properties. From the bottom to the top interval, the lithology of the O<sub>3</sub>w-S<sub>1</sub>l Formation changes from siliceous shale to argillaceous shale. Overall, the content of hard minerals increases with increasing depth on cores, while the clay content decreases.

Moreover, the host-rock facies also control the interface frequency. The frequent volcanic events and anoxic water environment promoted the formation of extensive thin k-bentonite and pyrite layers in the bottom interval; The data (Figs. 3 and 4) indicate that pyrite is more abundant at the bottom interval and exists in the form of thin laminae. Therefore, we can infer that the bottom of the O<sub>3</sub>w-S<sub>1</sub>l Formation has a strong degree of mechanical contrast across bedding, and this can promote the formation of small-scale and high-density bed-normal extension fractures, also provide many weak planes for bed-parallel sliding shear (Figs. 3 and 4).

Bed-parallel veins are the result of tensile fracturing and vertical dilation, with the fluid pressure exceeding lithostatic pressure in the compressional regime. (Wang et al., 2022). The formation mechanisms of overpressure include many processes, for example, during exhumation, thermal expansion of fluids, a de-watering reaction, and oil maturation (Tingay et al., 2009; Guo et al., 2016; Gao et al., 2019; Bons et al., 2022). Previous studies reported that the association between bed-parallel cracking and hydrocarbon generation in organic-rich shale may be common (Cobbald et al., 2013; Wang et al., 2020).

Additionally, the TOC and the degree of maturity show a positive correlation with the number of bed-parallel veins within a same sequence stratigraphy Larmier et al. (2021); Wang et al. (2022) confirmed that the paleo-pressure during the formation of bed-parallel fractures exceeded the lithostatic pressure through the inclusion temperature measurement and Raman technology. For organic-rich shale, oil maturation may be the main mechanism to trigger the cracking of bedding planes. The elevated maturity of organic matter causes the transformation of solid kerogen into liquid and gaseous hydrocarbons. With the increase of fluid volume expansion and fluid pressure, overpressure is finally generated in the low permeability shale.

We found that the vertical heterogeneous distribution of BPV seems to be related to the organic carbon content, and the location of BPV is significantly concentrated in the high TOC interval, similar to the observations of Wilkins et al. (2014) for the Marcellus shale in the Appalachian Basin, USA. The BPV location from the eight wells are compared with TOC indicator parameters (Fig. 14a and b) from the same intervals as available, including laboratory-measured TOC (TOC<sub>lab</sub>) and calculated well-log TOC (TOC<sub>log</sub>). The datasets (Fig. 14c) show that more than 70% of BPV occur in the interval with TOC greater than 3.5 %, in

agreement with the observations and distribution in the Vaca Muerta Formation core in Argentina (Larmier et al., 2021), revealing the important association between the BPV and total organic carbon content. Although the sampling interval (1-m spacing) of TOC<sub>lab</sub> will cause scattering, the cumulative curves of the two datasets are similar (Fig. 14c), so we speculate that the high TOC layers control the location of BPV in the study area.

## 5.2. Heterogeneous distribution of fractures

Our investigation shows different fracture patterns in two blocks. Several solutions can explain such differences in fracture distribution inside the Qiyue-Huaying Fold-Thrust belt. The first solution is that extensive shear fractures mainly result from strong deformation intensity. The deformation in the Qiyue-Huaying Fold-Thrust belt may develop in a progressively forward propagation from the Xuefeng uplift domain to the Huaying fault (Fig. 1). Consequently, total strain, fracture density, and the scale of resulting structures increase from distal foreland positions towards the internal zones of mountain belts. The apatite fission track data provide direct evidence and suggest that the initial uplift time of the Luzhou Block is late, about 40–50 Ma, while the Fuling Block is about 60–75 Ma (He et al., 2018; Li et al., 2020), therefore, the observed appearance corresponds to the main structural styles in both areas, with the Fuling Block exhibiting narrow and steep anticlines, while the Luzhou Block exhibits wide and gentle synclines (Fig. 1c and d). Shear fractures are formed under elevated differential stress during tectonic events, contrarily, extension fractures prefer to form under low differential stress; extension fractures may form during uplift as a result of thermal and elastic contraction (Engelder, 1993). Generally, the strong deformation induced extensive opening-mode large-scale fractures related to folds in the Fuling Block, compared to the Luzhou Block.

There are more abundant partly sealed bed-normal fractures in the Fuling block, with retained porosity continuously open to present. Burial depth might explain the abundant barren fractures in the Fuling Block since barren or partly sealed fractures mainly occur in shallow (cool) environments with minimal effects of synekinematic cementation or chemically assisted cracking (Hooker et al., 2023). Additionally, high-intensity tectonic events during uplift may also reactivate the pre-existing mineralized fractures with low cohesion, further improving fracture porosity. The widespread reactivation and opening of fracture set syn- or post-date the gas generation can provide conduits of gas leakage.

There is a difference in the development of BPV between the two blocks. The oblique fibers calcite crystal and inclusions recorded in BPV confirm that they formed at the maximum burial depth with fluid pressure (> 175 MPa) exceeding lithostatic pressure (Wang et al., 2022; Tang et al., 2024) (Fig. 15a), followed by an uplift stage. We collected the present fluid pressure data at the bottom interval of the O<sub>3</sub>w-S<sub>1</sub>l

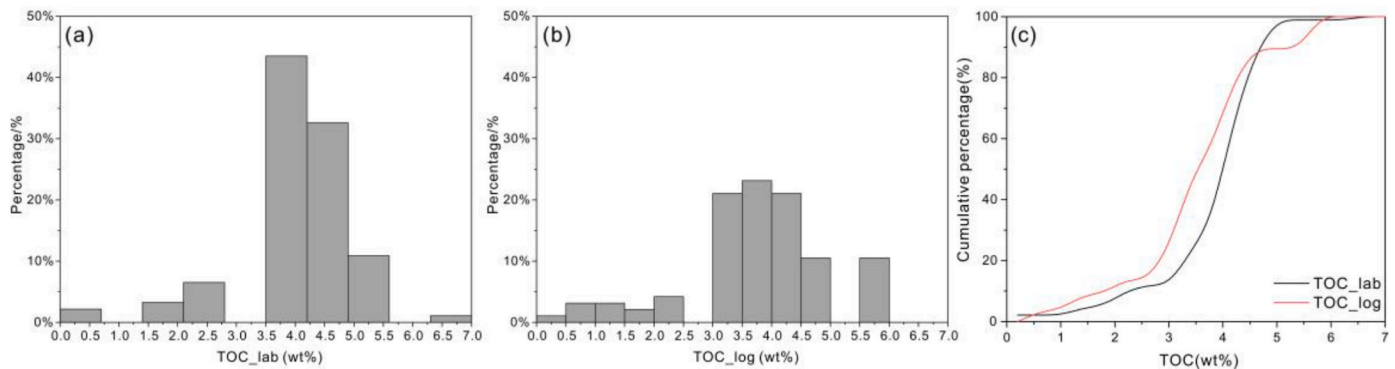


**Fig. 14.** The relationship between the TOC and the location of bed-parallel veins. (a–b) The TOC values of the location of bed-parallel veins. TOC<sub>lab</sub> represents the discrete TOC measured in the laboratory and TOC<sub>log</sub> represents the continuous TOC calculated from the well-log curve. (c) Cumulative curve of TOC values of the location of bed-parallel veins.

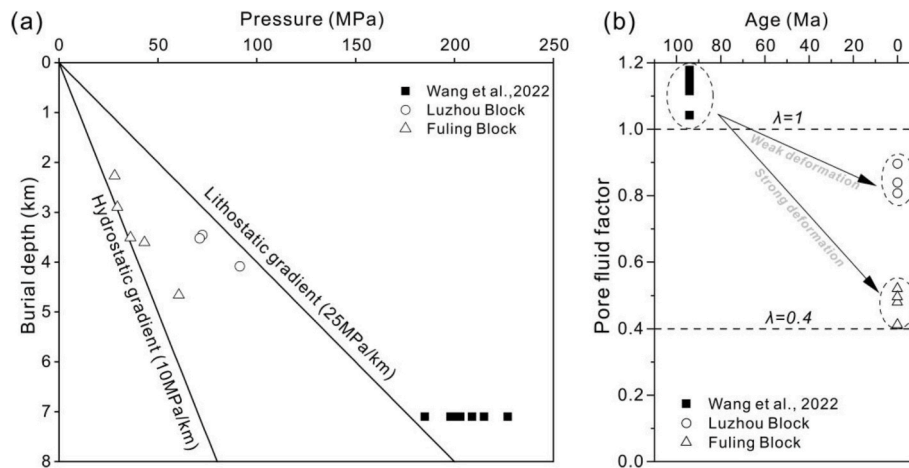


**Fig. 15.** The present fluid pressure and paleo-pressure plotted against burial depth. (a) The solid black rectangles from (Wang et al., 2022) represent the calculated trapping pressures in maximum burial depth during the Cretaceous, hollow circles and triangles corresponding to the present pore fluid factors of the Luzhou and Fuling Block. (b) The dashed line represents the pore fluid factor, i.e. the ratio of pore fluid pressure and vertical stress. The present pore fluid pressures are measured from well tests and drilling operations.

Formation (Table 1 and Fig. 15b), and found that the pore fluid factors ( $\lambda$ ) in the strong deformation (Fuling Block) area near the basin margin range from 0.41 to 0.52, which indicate that abundant fractures occurred during the late Yanshan-Himalayan period, and accompanied by overpressure leakage. The pore fluid factors of the weak deformation area (Luzhou Block) range from 0.81 to 0.90, indicating that it has retained the overpressure since the Cretaceous.

Strong compression in uplift stage caused a sharp decrease in fluid overpressure in the Fuling Block (Gao et al., 2019). Such low fluid overpressure cannot exceed the overburden pressure, resulting in the inability to induce bed-parallel fracturing of shale. However, relatively low compression occurred in the Luzhou Block, resulting in fluid overpressure retention since the Cretaceous (Cui et al., 2023). Therefore, the reduction of BPV in the strong deformation zone can be explained as the result of overpressure leakage in our study area. Generally, we speculate that the dominant origin of fractures changes from tectonic events to fluid pressure changes due to organic maturation (organic events), from the Fuling Block to the Luzhou Block.

The multi-stage structural superposition can affect fracture strikes. SN-striking regional faults occur in the Fuling Block and cut through the NE-striking regional faults, revealing that this area has experienced at least two stages of tectonic movements since the Late Jurassic: (1) the SE compression in Late Cretaceous (Yanshanian orogeny) formed the NE-striking thrust structure; (2) the EW compression formed the SN-striking regional faults during the Himalayan orogeny. However, only NE-striking regional faults occur in the Luzhou Block, indicating that fracture strikes in this area were mainly affected by the Yanshanian orogeny. Therefore, the development of EW-striking BNEFs, NEE-striking ISFs, and NWW-striking ISFs in the Fuling Block (Fig. 12) can be explained as the result of regional EW compression during the Himalayan orogeny. In general, the analysis of fracture attributes and their difference is helpful in evaluating the evolution of permeability and shale gas preservation.

## 6. Conclusions

Fracture investigation of eight cored deep wells, combined with TOC and mineralogy analysis inside the Qiyue-Huaying Fold-Thrust belt reveals how stratigraphy governs fracture occurrence and attributes. Our investigation suggests the following conclusions:

1. Four types of fractures have been identified, including bed-normal extension fracture, inclined shear fracture, bed-parallel shear

fracture, and bed-parallel mineral filled fracture (bed-parallel vein). The fracture pattern in the Fuling Block is characterized by steeply dipping opening-mode fractures and shear fractures (small faults), whereas the Luzhou Block is mainly characterized by abundant bed-parallel veins.

2. Host-rock facies chiefly controlled fracture occurrence. Fractures are preferentially localized in competent layers (siliceous shale with high TOC). Noteworthy, BPVs are systematically located in areas where shale layers have the highest TOC content (more than 70% of BPV is distributed in shale with TOC > 3.5 wt %), inferring a first-order link between the TOC and BPV distribution.
3. The dominant origin of fractures in organic-rich shale gradually changes from tectonic events to fluid pressure changes due to organic maturation (organic events), from the Fuling Block to the Luzhou Block.
4. There are differences inside the Qiyue-Huaying fold-thrust belt in terms of deformation intensity, burial depth, fluid pressure, and multi-directional stress superposition. These differences determine the type and attributes of fractures in the two blocks.

## CRedit authorship contribution statement

**Shijie Ma:** Writing – original draft, Methodology, Investigation, Formal analysis, Data curation, Conceptualization. **Lianbo Zeng:** Writing – review & editing, Supervision, Software, Project administration, Methodology, Funding acquisition, Conceptualization. **Marta Gasparrini:** Writing – review & editing. **Shiqiang Liu:** Investigation, Data curation. **Zhikai Liang:** Investigation, Data curation. **He Tian:** Investigation, Data curation. **Hanyong Bao:** Resources. **Wei Wu:** Resources. **Liang Luo:** Investigation, Data curation.

## Declaration of competing interest

The authors declare that they have no known competing financial interests or personal relationships that could have appeared to influence the work reported in this paper.

## Data availability

Data will be made available on request.



## Acknowledgements

This work was supported by the National Natural Science Foundation of China (Grant No. U1663203). The authors would like to thank four anonymous reviewers for their positive remarks and improvements. Aspects of this study were supported by Shale Gas Research Institute of PetroChina Southwest Oil and Gas field Company and Research Institute of Petroleum Exploration and Development of Jiangnan Oilfield Company.

## References

- Bons, P.D., Cao, D., Riese, T. de, González-Esvertit, E., Koehn, D., Naaman, I., Sachau, T., Tian, H., Gomez-Rivas, E., 2022. A review of natural hydrofractures in rocks. *Geol. Mag.* 1–26. <https://doi.org/10.1017/S0016756822001042>.
- Bons, P.D., Elburg, M.A., Gomez-Rivas, E., 2012. A review of the formation of tectonic veins and their microstructures. *J. Struct. Geol.* 43, 33–62. <https://doi.org/10.1016/j.jsg.2012.07.005>.
- Cao, Y., Xu, Q., Zheng, J., Tan, X., Li, M., Kershaw, S., Li, L., Qiu, Y., Deng, W., 2023. Two stages of late cretaceous to neogene deformation of the huayingshan tectonic belt, eastern Sichuan Basin, SW China. *J. Asian Earth Sci.* 255, 105779 <https://doi.org/10.1016/j.jseae.2023.105779>.
- Caswell, T.E., Milliken, R.E., 2017. Evidence for hydraulic fracturing at Gale crater, Mars: implications for burial depth of the Yellowknife Bay formation. *Earth Planet Sci. Lett.* 468, 72–84. <https://doi.org/10.1016/j.epsl.2017.03.033>.
- Cobbold, P.R., Zanella, A., Rodrigues, N., Løseth, H., 2013. Bedding-parallel fibrous veins (beef and cone-in-cone): worldwide occurrence and possible significance in terms of fluid overpressure, hydrocarbon generation and mineralization. *Mar. Petrol. Geol.* 43, 1–20. <https://doi.org/10.1016/j.marpetgeo.2013.01.010>.
- Cui, Y., Li, X., Guo, W., Lin, W., Hu, Y., Han, L., Qian, C., Zhao, J., 2023. Enlightenment of calcite veins in deep Ordovician Wufeng–Silurian Longmaxi shales fractures to migration and enrichment of shale gas in southern Sichuan Basin, SW China. *Petrol. Explor. Dev.* 50, 1374–1385. [https://doi.org/10.1016/S1876-3804\(24\)60473-8](https://doi.org/10.1016/S1876-3804(24)60473-8).
- Dai, J., Zou, C., Liao, S., Dong, D., Ni, Y., Huang, J., Wu, W., Gong, D., Huang, S., Hu, G., 2014. Geochemistry of the extremely high thermal maturity Longmaxi shale gas, southern Sichuan Basin. *Org. Geochem.* 74, 3–12. <https://doi.org/10.1016/j.ORGEOCHEM.2014.01.018>.
- Deng, B., Li, Z.W., Liu, S.G., Wang, G.Z., Li, S.J., Qin, Z.P., Li, J.X., Jansa, L., 2016. Structural geometry and kinematic processes at the intracontinental Daloushan mountain chain: implications for tectonic transfer in the Yangtze Block interior. *Compt. Rendus Geosci.* 348, 159–168. <https://doi.org/10.1016/j.crte.2015.06.009>.
- Engelder, T., Lash, G.G., Uzcátegui, R.S., 2009. Joint sets that enhance production from middle and upper devonian gas shales of the Appalachian Basin. *AAPG (Am. Assoc. Pet. Geol.) Bull.* 93, 857–889. <https://doi.org/10.1306/03230908032>.
- Engelder, T., Peacock, D.C.P., 2001. Joint development normal to regional compression during flexural-flow folding: the Lillstock buttress anticline, Somerset, England. *J. Struct. Geol.* 23, 259–277. [https://doi.org/10.1016/S0191-8141\(00\)00095-X](https://doi.org/10.1016/S0191-8141(00)00095-X).
- English, J.M., Laubach, S.E., 2017. Opening-mode fracture systems: insights from recent fluid inclusion microthermometry studies of crack-seal fracture cements. *Geol. Soc. Spec. Publ.* 458 (1), 257–272. <https://doi.org/10.1144/SP458>.
- Fall, A., Eichhubl, P., Cumella, S.P., Bodnar, R.J., Laubach, S.E., Becker, S.P., 2012. Testing the basin-centered gas accumulation model using fluid inclusion observations: Southern Piceance Basin, Colorado. *AAPG (Am. Assoc. Pet. Geol.) Bull.* 96, 2297–2318. <https://doi.org/10.1306/05171211149>.
- Feng, Q., Qiu, N., Borjigin, T., Wu, H., Zhang, J., Shen, B., Wang, J., 2022. Tectonic evolution revealed by thermo-kinematic and its effect on shale gas preservation. *Energy* 240. <https://doi.org/10.1016/j.energy.2021.122781>.
- Gale, J.F.W., Laubach, S.E., Olson, J.E., Eichhubl, P., Fall, A., 2014. Natural fractures in shale: a review and new observations. *AAPG (Am. Assoc. Pet. Geol.) Bull.* 101, 2165–2216. <https://doi.org/10.1306/08121413151>.
- Gao, J., Zhang, J., Kun, He, S., Zhao, J., Xin, He, Z., Liang, Wo, Jin, Y., Feng, Y., Xing, Li, W., 2019. Overpressure generation and evolution in Lower Paleozoic gas shales of the Jiaoshiba region, China: implications for shale gas accumulation. *Mar. Petrol. Geol.* 102, 844–859. <https://doi.org/10.1016/j.marpetgeo.2019.01.032>.
- Gasparrini, M., Lacombe, O., Rohais, S., Belkacemi, M., Euzen, T., 2021. Natural mineralized fractures from the Montney-Doig unconventional reservoirs (Western Canada Sedimentary Basin): timing and controlling factors. *Mar. Petrol. Geol.* 124, 104826. <https://doi.org/10.1016/j.marpetgeo.2020.104826>.
- Ge, X., Shen, C., Selby, D., Deng, D., Mei, L., 2016. Apatite fission-track and Re-Os geochronology of the xuefeng uplift, China: temporal implications for dry gas associated hydrocarbon systems. *Geology* 44, 491–494. <https://doi.org/10.1130/G37666.1>.
- Gu, Z., Wang, X., Nunns, A., Zhang, B., Jiang, H., Fu, L., Zhai, X., 2021. Structural styles and evolution of a thin-skinned fold-and-thrust belt with multiple detachments in the eastern Sichuan Basin, South China. *J. Struct. Geol.* 142, 104191. <https://doi.org/10.1016/j.jsg.2020.104191>.
- Guo, X., 2019. Major factors controlling the shale gas accumulations in Wufeng–Longmaxi Formation of the pingqiao shale gas field in fuling area, Sichuan Basin, China. *J. Nat. Geosci.* 4, 129–138. <https://doi.org/10.1016/j.jngs.2019.06.002>.
- Guo, X., Liu, K., Jia, C., Song, Y., Zhao, M., Zhuo, Q., Lu, X., 2016. Constraining tectonic compression processes by reservoir pressure evolution: overpressure generation and evolution in the Kelasu Thrust Belt of Kuqa Foreland Basin, NW China. *Mar. Petrol. Geol.* 72, 30–44. <https://doi.org/10.1016/j.marpetgeo.2016.01.015>.
- Hantschel, T., Kauer, A.L., 2009. Fundamentals of basin and petroleum systems modeling. *Fundamentals of Basin and Petroleum Systems Modeling*, pp. 1–476. <https://doi.org/10.1007/978-3-540-72318-9>.
- Hao, X., Wen, Z., Qin, H., Ting, Y., Jiang, K., Ankun, Z., Zihui, L., Yu, Y., 2021. Quartz types, silica sources and their implications for porosity evolution and rock mechanics in the Paleozoic Longmaxi Formation shale, Sichuan Basin. *Mar. Petrol. Geol.* 128, 105036. <https://doi.org/10.1016/j.marpetgeo.2021.105036>.
- He, W., Zhou, J., Yuan, K., 2018. Deformation evolution of eastern sichuan–xuefeng fold-thrust belt in south China: insights from analogue modelling. *J. Struct. Geol.* 109, 74–85. <https://doi.org/10.1016/j.jsg.2018.01.002>.
- Holland, M., Urai, J.L., 2010. Evolution of anastomosing crack-seal vein networks in limestones: insight from an exhumed high-pressure cell, Jabal Shams, Oman Mountains. *J. Struct. Geol.* 32, 1279–1290. <https://doi.org/10.1016/j.jsg.2009.04.011>.
- Hooker, J.N., Katz, R.F., Laubach, S.E., Cartwright, J., Eichhubl, P., Ukar, E., Bloomfield, D., Engelder, T., 2023. Fracture-pattern growth in the deep, chemically reactive subsurface. *J. Struct. Geol.* 173, 104915. <https://doi.org/10.1016/j.jsg.2023.104915>.
- Hooker, J.N., Laubach, S.E., Marrett, R., 2013. Fracture-aperture sizedfrequency, spatial distribution, and growth processes in strata-bounded and non-strata-bounded fractures, cambrian mesón group, NW Argentina. *J. Struct. Geol.* 54, 54–71. <https://doi.org/10.1016/j.jsg.2013.06.011>.
- Huang, H., He, D., Li, Y., Li, J., Zhang, L., 2018. Silurian tectonic-sedimentary setting and basin evolution in the Sichuan area, southwest China: implications for palaeogeographic reconstructions. *Mar. Petrol. Geol.* 92, 403–423. <https://doi.org/10.1016/j.marpetgeo.2017.11.006>.
- Huang, Z., Li, Z., Shi, W., Yang, X., Wang, X., Young, S., 2023. Differential sedimentary mechanisms of upper ordovician-lower silurian shale in southern Sichuan Basin, China. *Mar. Petrol. Geol.* 148, 106040. <https://doi.org/10.1016/j.marpetgeo.2022.106040>.
- Hunt, J.M., 1990. Generation and migration of petroleum from abnormally pressured fluid compartments. *AAPG (Am. Assoc. Pet. Geol.) Bull.* 74, 1–12. <https://doi.org/10.1306/0C9B21EB-1710-11D7-8645000102C1865D>.
- Ilgner, A.G., Heath, J.E., Akkutlu, I.Y., Bryndzia, L.T., Cole, D.R., Kharaka, Y.K., Kneafsey, T.J., Milliken, K.L., Pyrak-Nolte, L.J., Suarez-Rivera, R., 2017. Shales at all scales: exploring coupled processes in mudrocks. *Earth Sci. Rev.* 166, 132–152. <https://doi.org/10.1016/j.earscirev.2016.12.013>.
- Labani, M.M., Rezaee, R., 2015. The importance of geochemical parameters and shale composition on rock mechanical properties of gas shale reservoirs: a case study from the kockatea shale and caryginia formation from the perth basin, western Australia. *Rock Mech. Rock Eng.* 48, 1249–1257. <https://doi.org/10.1007/S00603-014-0617-6>.
- Larmier, S., Zanella, A., Lejay, A., Mourgues, R., Gelin, F., 2021. Geological parameters controlling the bedding-parallel vein distribution in Vaca Muerta Formation core data, Neuquén Basin, Argentina. *AAPG (Am. Assoc. Pet. Geol.) Bull.* 105, 2221–2243. <https://doi.org/10.1306/03122119201>.
- Laubach, S.E., Olson, J.E., Cross, M.R., 2009. Mechanical and fracture stratigraphy. *AAPG (Am. Assoc. Pet. Geol.) Bull.* 93, 1413–1426. <https://doi.org/10.1306/07270909094>.
- Laubach, S.E., Reed, R.M., Olson, J.E., Lander, R.H., Bonnell, L.M., 2004. Coevolution of crack-seal texture and fracture porosity in sedimentary rocks: cathodoluminescence observations of regional fractures. *J. Struct. Geol.* 26, 967. <https://doi.org/10.1016/j.jsg.2003.08.019>.
- Lazar, O.R., Bohacs, K.M., Macquaker, J.H.S., Schieber, J., Demko, T.M., 2015. Capturing key attributes of fine-grained sedimentary rocks in outcrops, cores, and thin sections: nomenclature and description guidelines. *J. Sediment. Res.* 85, 230–246. <https://doi.org/10.2110/JSR.2015.11>.
- Li, S., Li, Y., He, Z., Chen, K., Zhou, Y., Yan, D., 2020. Differential deformation on two sides of Qiyueshan Fault along the eastern margin of Sichuan Basin, China, and its influence on shale gas preservation. *Mar. Petrol. Geol.* 121, 104602. <https://doi.org/10.1016/j.marpetgeo.2020.104602>.
- Li, Y., Chen, X., Shao, Y., 2023. 3D natural fracture model of shale reservoir based on petrophysical characterization. *J. Struct. Geol.* 166, 104763. <https://doi.org/10.1016/j.jsg.2022.104763>.
- Li, Y., He, J., Deng, H., Li, R., Li, Q., Fu, M., Yu, Y., 2024. Effect of lithofacies assemblages on multi-scale fractures in the transitional shale and its implications for shale gas exploration. *Geoenery Sci. Eng.* 233, 212562. <https://doi.org/10.1016/j.GEOEN.2023.212562>.
- Liu, S., Deng, B., Zhong, Y., Ran, B., Yong, S., Sun, W., Yang, D., Jiang, L., Ye, Y., 2016. Unique geological features of burial and superimposition of the Lower Paleozoic shale gas across the Sichuan Basin and its periphery. *Earth Sci. Front.* 23, 11–28. <https://doi.org/10.13745/J.ESF.2016.01.002>.
- Liu, S., Yang, Y., Deng, B., Zhong, Y., Wen, L., Sun, W., Li, Z., Jansa, L., Li, J., Song, J., Zhang, X., Peng, H., 2021. Tectonic evolution of the Sichuan Basin, southwest China. *Earth Sci. Rev.* 213. <https://doi.org/10.1016/j.earscirev.2020.103470>.
- Ma, S., Zeng, L., Tian, H., Shi, X., Wu, W., Yang, S., Luo, L., Xu, X., 2023. Fault damage zone and its effect on deep shale gas: insights from 3D seismic interpretation in the southern Sichuan Basin, China. *J. Struct. Geol.* 170. <https://doi.org/10.1016/j.jsg.2023.104848>.
- Ma, X., Wang, H., Zhou, S., Feng, Z., Liu, H., Guo, W., 2020. Insights into NMR response characteristics of shales and its application in shale gas reservoir evaluation. *J. Nat. Gas Sci. Eng.* 84. <https://doi.org/10.1016/j.jngse.2020.103674>.



- Ma, X., Xie, J., 2018. The progress and prospects of shale gas exploration and development in southern Sichuan Basin, SW China. *Petrol. Explor. Dev.* 45, 172–182. [https://doi.org/10.1016/S1876-3804\(18\)30018-1](https://doi.org/10.1016/S1876-3804(18)30018-1).
- Ma, Z., Tan, J., Zheng, L., Shen, B., Wang, Z., Shahzad, A., Jan, I.U., Schulz, H.M., 2021. Evaluating gas generation and preservation of the Wufeng-Longmaxi Formation shale in southeastern Sichuan Basin, China: implications from semiclosed hydrous pyrolysis. *Mar. Petrol. Geol.* 129 <https://doi.org/10.1016/j.marpetgeo.2021.105102>.
- Meng, Q., Hao, F., Tian, J., 2021. Origins of non-tectonic fractures in shale. *Earth Sci. Rev.* 222, 103825 <https://doi.org/10.1016/J.EARSCIREV.2021.103825>.
- Meng, Q., Hooker, J., Cartwright, J., 2018. Lithological control on fracture cementation in the keuper marl (triassic), north somerset, UK. *Geol. Mag.* 155, 1761–1775. <https://doi.org/10.1017/S001675681700070X>.
- Peacock, D.C.P., Mann, A., 2005. Evaluation of the controls on fracturing in reservoir rocks. *J. Petrol. Geol.* 28, 385–396. <https://doi.org/10.1111/J.1747-5457.2005.TB00089.X>.
- Pei, P., Ling, K., Hou, X., Nordeng, S., Johnson, S., 2016. Brittleness investigation of producing units in Three Forks and bakken formations, williston basin. *J. Nat. Gas Sci. Eng.* 32, 512–520. <https://doi.org/10.1016/j.jngse.2016.04.053>.
- Peng, J., Milliken, K.L., Fu, Q., 2020. Quartz types in the Upper Pennsylvanian organic-rich Cline Shale (Wolfcamp D), Midland Basin, Texas: implications for silica diagenesis, porosity evolution and rock mechanical properties. *Sedimentology* 67, 2040–2064. <https://doi.org/10.1111/SED.12694>.
- Ramsay, J.G., 1980. The crack-seal mechanism of rock deformation. *Nature* 284, 135–139. <https://doi.org/10.1038/284135A0>.
- Ravier, E., Martinez, M., Pellenard, P., Zanella, A., Tupinier, L., 2020. The milankovitch fingerprint on the distribution and thickness of bedding-parallel veins (beef) in source rocks. *Mar. Petrol. Geol.* 122 <https://doi.org/10.1016/j.marpetgeo.2020.104643>.
- Rodrigues, N., Cobbold, P.R., Loseth, H., Ruffet, G., 2009. Widespread bedding-parallel veins of fibrous calcite ("beef") in a mature source rock (Vaca Muerta Fm, Neuquén Basin, Argentina): evidence for overpressure and horizontal compression. *J. Geol. Soc.* 166, 695–709. <https://doi.org/10.1144/0016-76492008-111>.
- Romero-Sarmiento, M.F., Ducros, M., Carpentier, B., Lorient, F., Cacas, M.C., Pegaz-Fiornet, S., Wolf, S., Rohais, S., Moretti, I., 2013. Quantitative evaluation of TOC, organic porosity and gas retention distribution in a gas shale play using petroleum system modeling: application to the Mississippian Barnett Shale. *Mar. Petrol. Geol.* 45, 315–330. <https://doi.org/10.1016/J.MARPETGEO.2013.04.003>.
- Shangbin, C., Yanming, Z., Si, C., Yufu, H., Changqing, F., Junhua, F., 2017. Hydrocarbon generation and shale gas accumulation in the Longmaxi Formation, southern Sichuan Basin, China. *Mar. Petrol. Geol.* 86, 248–258. <https://doi.org/10.1016/j.marpetgeo.2017.05.017>.
- Tang, L., Wang, P., Zhao, Z., Song, Y., Chen, X., Jiang, Z., Jiang, S., Li, Q., Li, X., 2024. Overpressure origin and evolution during burial in the shale gas plays of the Wufeng-Longmaxi formations of southern Sichuan basin. *Geoenergy Sci. Eng.* 236, 212729 <https://doi.org/10.1016/J.GEOEN.2024.212729>.
- Tian, H., Zeng, L., Ma, S., Li, H., Mao, Z., Peng, Y., Xu, X., Feng, D., 2022. Effects of different types of fractures on shale gas preservation in Lower Cambrian shale of northern Sichuan Basin: evidence from macro-fracture characteristics and microchemical analysis. *J. Petrol. Sci. Eng.* 218, 110973 <https://doi.org/10.1016/J.PETROL.2022.110973>.
- Tingay, M.R.P., Hillis, R.R., Swarbrick, R.E., Morley, C.K., Damit, A.R., 2009. Origin of overpressure and pore-pressure prediction in the Baram province, Brunei. *AAPG (Am. Assoc. Pet. Geol.) Bull.* 93, 51–74. <https://doi.org/10.1306/08080808016>.
- Tuo, J., Wu, C., Zhang, M., 2016. Organic matter properties and shale gas potential of Paleozoic shales in Sichuan Basin, China. *J. Nat. Gas Sci. Eng.* 28, 434–446. <https://doi.org/10.1016/j.jngse.2015.12.003>.
- Ukar, E., Lopez, R.G., Gale, J.F.W., Laubach, S.E., Mancada, R., 2017. New type of kinematic indicator in bed-parallel veins, late jurassic–early cretaceous Vaca Muerta Formation, Argentina: E-W shortening during late cretaceous vein opening. *J. Struct. Geol.* 104, 31–47. <https://doi.org/10.1016/j.jsg.2017.09.014>.
- Wang, M., Chen, Y., Bain, W.M., Song, G., Liu, K., Zhou, Z., Steele-MacInnis, M., 2020. Direct evidence for fluid overpressure during hydrocarbon generation and expulsion from organic-rich shales. *Geology* 48, 374–378. <https://doi.org/10.1130/G46650.1>.
- Wang, X., Hu, W., Qiu, Y., Liu, Y., Jia, D., Cao, J., Liu, X., Li, Y., 2022. Fluid inclusion evidence for extreme overpressure induced by gas generation in sedimentary basins. *Geology* 50 (1), 765–770. <https://doi.org/10.1130/G49848>.
- Wang, X., Wang, R., Ding, W., Yin, S., Sun, Y., Zhou, X., Li, Q., 2017. Development characteristics and dominant factors of fractures and their significance for shale reservoirs: a case study from C1b2 in the Cen'gong block, southern China. *J. Petrol. Sci. Eng.* 159, 988–999. <https://doi.org/10.1016/J.PETROL.2017.08.007>.
- Weger, R.J., Murray, S.T., McNeill, D.F., Swart, P.K., Eberli, G.P., Rodriguez Blanco, L., Tenaglia, M., Rueda, L.E., 2019. Paleothermometry and distribution of calcite beef in the Vaca Muerta Formation, neuquén basin, Argentina. *AAPG (Am. Assoc. Pet. Geol.) Bull.* 103, 931–950. <https://doi.org/10.1306/10021817384>.
- Wilkins, S., Mount, V., Mahon, K., Perry, A., Koenig, J., 2014. Characterization and development of subsurface fractures observed in the Marcellus Formation, Appalachian Plateau, north-central Pennsylvania. *AAPG (Am. Assoc. Pet. Geol.) Bull.* 98, 2301–2345. <https://doi.org/10.1306/08191414024>.
- Xu, S., Gou, Q., Hao, F., Zhang, B., Shu, Z., Zhang, Y., 2020. Multiscale faults and fractures characterization and their effects on shale gas accumulation in the Jiaoshiba area, Sichuan Basin, China. *J. Petrol. Sci. Eng.* 189, 107026 <https://doi.org/10.1016/J.PETROL.2020.107026>.
- Xu, X., Zeng, L., Tian, H., Ling, K., Che, S., Yu, X., Shu, Z., Dong, S., 2021. Controlling factors of lamellation fractures in marine shales: a case study of the Fuling area in Eastern Sichuan Basin, China. *J. Petrol. Sci. Eng.* 207 <https://doi.org/10.1016/j.petrol.2021.109091>.
- Zanella, A., Cobbold, P.R., Rodrigues, N., Løseth, H., Jolivet, M., Gouttefangeas, F., Chew, D., 2021. Source rocks in foreland basins: a preferential context for the development of natural hydraulic fractures. *AAPG (Am. Assoc. Pet. Geol.) Bull.* 105, 647–668. <https://doi.org/10.1306/08122018162>.
- Zanella, A., Cobbold, P.R., Ruffet, G., Leanza, H.A., 2015. Geological evidence for fluid overpressure, hydraulic fracturing and strong heating during maturation and migration of hydrocarbons in Mesozoic rocks of the northern Neuquén Basin, Mendoza Province, Argentina. *J. S. Am. Earth Sci.* 62, 229–242. <https://doi.org/10.1016/J.JSAMES.2015.06.006>.
- Zeng, L., Lyu, W., Li, J., Zhu, L., Weng, J., Yue, F., Zu, K., 2016. Natural fractures and their influence on shale gas enrichment in Sichuan Basin, China. *J. Nat. Gas Sci. Eng.* 30, 1–9. <https://doi.org/10.1016/j.jngse.2015.11.048>.
- Zeng, L., Shu, Z., Lyu, W., Zhang, M., Bao, H., Dong, S., Chen, S., Xu, X., 2021. Lamellation fractures in the paleogene continental shale oil reservoirs in the qianjiang depression, jiangnan basin, China. *Geofluids*. <https://doi.org/10.1155/2021/6653299>, 2021.
- Zeng, W., Zhang, J., Ding, W., Zhao, S., Zhang, Y., Liu, Z., Jiu, K., 2013. Fracture development in Paleozoic shale of Chongqing area (South China). Part one: fracture characteristics and comparative analysis of main controlling factors. *J. Asian Earth Sci.* 75, 251–266. <https://doi.org/10.1016/j.jseas.2013.07.014>.
- Zhang, J., Li, X., Xie, Z., Li, J., Zhang, X., Sun, K., Wang, F., 2018. Characterization of microscopic pore types and structures in marine shale: examples from the upper permian dalong formation, northern Sichuan Basin, south China. *J. Nat. Gas Sci. Eng.* 59, 326–342. <https://doi.org/10.1016/j.jngse.2018.09.012>.
- Zhang, X., Wang, R., Shi, W., Hu, Q., Xu, X., Shu, Z., Yang, Y., Feng, Q., 2023. Structure- and lithofacies-controlled natural fracture developments in shale: implications for shale gas accumulation in the Wufeng-Longmaxi Formations, Fuling Field, Sichuan Basin, China. *Geoenergy Sci. Eng.* 223, 211572 <https://doi.org/10.1016/J.GEOEN.2023.211572>.
- Zou, C., Yang, Z., Dai, J., Dong, D., Zhang, B., Wang, Y., Deng, S., Huang, J., Liu, K., Yang, C., Wei, G., Pan, S., 2015. The characteristics and significance of conventional and unconventional Sinian-Silurian gas systems in the Sichuan Basin, central China. *Mar. Petrol. Geol.* 64, 386–402. <https://doi.org/10.1016/j.marpetgeo.2015.03.005>.
- Zou, C., Zhao, Q., Cong, L., Wang, H., Shi, Z., Wu, J., Pan, S., 2021. Development progress, potential and prospect of shale gas in China. *Nat. Gas. Ind.* 41, 1–14. <https://doi.org/10.3787/J.ISSN.1000-0976.2021.01.001>.